



# The effect of hot isostatic pressing pressure level and solution annealing cooling rate on CM247 LC nickel-based superalloy processed by laser-based powder bed fusion

P. A. Martelli<sup>1,2</sup> · E. Bassini<sup>1,2,3</sup> · D. Ugues<sup>1,2,3</sup>

Received: 6 September 2023 / Accepted: 26 April 2024  
© The Author(s) 2024

## Abstract

In the present work, CM247 LC samples produced by laser-based powder bed fusion (PBF-LB) were heat treated inside a hot isostatic pressing (HIP) furnace (HIP quench treatment) at 1260 °C for 3 h to combine the solution annealing with the elimination of defects of the additively manufactured parts. In particular, the effects of different applied pressures (50–170 MPa) and cooling rates (from 162 to 2450 °C/min) on the final densification, grain coarsening, and  $\gamma'$  precipitation were studied. The results were also compared to a sample heat treated in a low-pressure furnace and gas-quenched at 195 °C/min. The study revealed that the applied pressure has a negligible effect on densification, grain coarsening, and the size and shape of  $\gamma'$ , which is always irregular after solution annealing, independently from the cooling rate. For this reason, first aging was subsequently applied at 1080 °C for 4 h to HIP-quenched samples, revealing that this step of treatment is effectively responsible for the final cubic shape of  $\gamma'$ , even if a starting irregular morphology is considered. Finally, additional samples were heat treated in an air furnace and air cooled to room temperature prior to the HIP quench; this procedure allowed assessing the solutioning effectiveness of the HIP quench with coarse precipitates typical of conventional processing (e.g., investment casting). Overall, this study underscores the efficacy of the HIP quench in enhancing microstructural attributes and mitigating defects, providing valuable insights for enhancing the properties of challenging Ni-based alloys fabricated through additive manufacturing techniques.

**Keywords** High-temperature alloys · Additive manufacturing · Microstructure · High pressure · Scanning electron microscopy (SEM)

## 1 Introduction

Nickel-based superalloys such as CM247 LC are typically used in the aeronautical and energy production sectors because of their outstanding thermo-mechanical properties and resistance to oxidation [1]. Additive manufacturing (AM) is gaining significant interest in producing complex

near net shape (NNS) parts due to the added value of the previous applications [2], and particular attention is being given to Laser-Based Powder Bed Fusion (PBF-LB) [3–7]. However, PBF-LB processed materials cope with issues intrinsically related to the process. More specifically, the material shows densification flaws after the printing stage. Generally, these defects can be divided into circular pores, generated by entrapped gas from the print or the atomization (gas porosities), larger voids caused by insufficient energy input with irregular shape and typically oriented transversal to the building direction (lack of fusion) and cracks, which can form due to different mechanisms: ductility dip cracking, liquation cracking, thermal cracking, or strain age cracking [8]. The high cooling rate inherent in PBF-LB processes is the root reason for obtaining a microstructure diverging significantly from those expected in traditional manufacturing: the  $\gamma'$  precipitation and growth is significantly biased toward nucleation, which leads to the formation of small reinforcing

✉ E. Bassini  
emilio.bassini@polito.it

<sup>1</sup> Dipartimento di Scienza Applicata e Tecnologia (DISAT), Politecnico di Torino, corso duca degli abruzzi 24, 10129 Turin, Italy

<sup>2</sup> Centro Interdipartimentale Integrated Additive Manufacturing IAM@PoliTO, Alessandria, Italy

<sup>3</sup> Consorzio Nazionale della Scienza e Tecnologia dei Materiali (INSTM), Florence, Italy

particles and negligible growth [3, 7]. The observation of these small particles is only demonstrated via TEM investigations as described in the work of Miller et al. [9]. At the same time, the strong thermal gradients generated during the manufacturing cause the formation of elongated grains parallel to the building direction, characterized by strong anisotropy.

For this reason, a tailored post-processing is required to solve the two abovementioned issues. Specifically, Hot Isostatic Pressing (HIP) can reduce the densification flaws exploiting the simultaneous application of high pressures and temperatures. The driving force for this solid-state diffusion process is the reduction in surface energy of the flaws [10]. Defects closure is obtained through a thermal diffusional process and a plastic flow of the material, aided by the application of an external pressure. After HIP, the alloy post-process requires a solution annealing and several aging steps. This process ensures that the shape, size, and fraction of  $\gamma'$  are compliant with the required mechanical properties of CM247 LC. According to the literature, Nickel-based superalloys can show, after heat treatment, spherical or cubic  $\gamma'$  particles depending on the lattice misfit between the FCC- $\gamma$  and L1<sub>2</sub>- $\gamma'$  cubic cells. According to Nguyen et al. [11], near-zero  $\gamma$ - $\gamma'$  lattice misfit leads to spherical precipitates, which become cubic when the lattice misfit reaches 0.5% up to 1%. Moreover, Van Sluytman et al. [12] found that the concentration of solute elements can affect such behavior, with Ta, W, and Cr promoting cubic-shaped particles. Finally, the  $\gamma'$  shape can degenerate into irregular and coarse fan-like structures due to process conditions or thermal exposure [13, 14].

In addition to  $\gamma'$  precipitation, the solution annealing is applied to fully recover the anisotropy and highly textured thin grains inherited by the PBF-LB process [7, 15, 16]. During the subsequent cooling to room temperature, nuclei of  $\gamma'$  form and grow due to the coexistent and not exclusive mechanisms of spinodal decomposition and chemical ordering [17]. Then first aging is applied below the  $\gamma'$  solvus to promote its growth into the thermally stable cubic shape [7]. Finally, a second aging is usually applied to reach the hardness peak of the alloy by promoting further precipitation of very fine tertiary  $\gamma'$  [13].

Therefore, it becomes attractive to combine the healing process of HIP and the heat treatment in a single optimized cycle within the same furnace. Such an approach is nowadays accessible thanks to the development of HIP furnaces equipped with high cooling rate units. This process, normally referred as to HIP quench, already proved to significantly reduce the total post-process time on different materials [18, 19]. Furthermore, the continuous application of the pressure during the heat treatment prevents the generation or the re-opening of pores during the soaking time at high temperature. In fact, it has been proved that HT performed

after HIP could lead to undesired porosities due to Kirkendall effect [20] or entrapped Argon expansion [21, 22]. A contingency should be avoided since it has adverse effects on the mechanical properties of Ni-based superalloys [23, 24]. Therefore, the possibility of merging HIP and HT for AM alloys is highly important to counter the formation of porosities during HT. Lopez-Galilea et al. [25] integrated the HT of a PBF-LB CMSX-4 alloy in a HIP furnace regarding AM Nickel superalloys. However, many cracks were still retained after applying the supersolvus HIP treatment. Similarly, a HIP-integrated HT was applied in Ref. [26] for a CMSX-4 alloy processed with Selective Electron Beam Melting (SEBM). Goel et al. [27] integrated HT in HIP for an EBM IN718 alloy, demonstrating the positive effect of this combination on both dissolution of undesired  $\delta$  phase and densification of manufacture defects.

Albeit HIP quench is industrially appealing when time savings are considered, it is still important to demonstrate that performing the solution annealing under high pressures on Ni-based superalloys still generates comparable results to those obtainable after a low-pressure heat treatment. In fact, at authors' best knowledge, only little research was done regarding this aspect, even if it has been proved that HIP pressure can generate unexpected microstructure. For example, differences on the austenite-pearlite transformation in steels were observed due to the effect of the applied pressure [28] or during the homogenization of a peritectic TiAl intermetallic [29]. Regarding  $\gamma'$  reinforced Nickel superalloys, the spotlight was placed especially on the time savings achievable with the integration of HIP and HT on cast single crystal (SX) alloys. Mujica Roncery et al. [30] successfully applied an integrated solution annealing and aging in HIP on an SX ERBO/1 alloy, demonstrating that a finer  $\gamma'$  with a slight increase in the volume fraction could be obtained with respect to the conventionally treated alloy. Moreover, the effect of the pressure and the cooling rate on the densification during HIP has been assessed, observing that low pressures could limit the densification level below 100%. In contrast, the cooling rates seem to have little or no effects on the densification. Lopez-Galilea et al. [31] investigated the possibility of applying a Super Solidus HIP (SSHIP) on a cast CMSX-10 alloy to recover the microstructural segregation from cast while reaching optimal densification levels, taking advantage of the higher diffusivity in the liquid phase ( $\gamma$ - $\gamma'$  eutectic) rather than in the solid. Nevertheless, at authors' best knowledge, no research work regarding additively manufactured Ni-based superalloys systematically compared the microstructures achievable by modulating the applied pressure and the cooling rate during the solution annealing, especially for CM247 LC, which contains high volume fraction of  $\gamma'$ .

In particular, this paper focuses on the assessment of the possible effects that pressure may introduce on flaws

densification, the  $\gamma'$  solutioning and precipitation process, along with the effect of the cooling rate on the microstructural features, integrating HT in HIP on a PBF-LB CM247 LC alloy. Specifically, as-built cubic samples underwent super-solvus HIP quench (HIP-Q) at 1260 °C under different operational conditions. Three different pressure levels (50–110–170 MPa) were used to assess the influence of this parameter on the densification flaws' healing process during HIP-Q and the resulting microstructure, for which a reference treatment in a low-pressure furnace was also performed under the same temperature and soaking time conditions. Moreover, two different modules were used in the HIP facility to provide different cooling rates. The first one allows for cooling rates up to 250 °C/min to study industrial-like treatment conditions, while the second can cool at several thousands of °C/min, to freeze the microstructure obtained at the end of the solution annealing. Furthermore, first aging after HIP-Q was also investigated to assess its role in defining the final  $\gamma'$  shape.

## 2 Materials and methods

### 2.1 Samples production

A pre-alloyed gas-atomized CM247 LC Nickel superalloy produced by Praxair Inc. and commercialized as NI-1230 was used. The powder was sieved from the manufacturer in the range of 16–45  $\mu\text{m}$ , and the nominal chemical composition is reported in Table 1.

Nine 20 mm cubic samples were produced in a Print-Sharp250 PBF-LB system by Prima Additive. A rubber recoater and a 250×250 mm low-carbon steel platform heated to 80 °C were used. The powder was processed with a stripescan strategy implying a stripe rotation of 67° between each layer. The process was conducted in a pure Ar atmosphere (oxygen content <0.1%). The ranges for the main process parameters are listed in Table 2.

### 2.2 Post-process and heat treatments

The as-built samples were removed from the building platform by wire electro-discharge machining (WEDM). After manual sandblasting, they underwent stress relief (SR) at 1080 °C for 2 h to eliminate the residual stresses from the printing stage. Then samples could follow different heat treatments, which are described as follows and schematically depicted in Fig. 1:

**Table 2** Ranges for the main process parameters

Laser power [W]	Scan speed [mm/s]	Hatching distance [mm]
170–195	1000–1900	0.03–0.08

- One sample underwent solution annealing in a low-pressure ( $10^{-2}$  mbar) TAV Minijet furnace at 1260 °C for 3 h and gas quenched at 1.5 bar (=195 °C/min).
- Five samples underwent HIP-Q in a Quintus QIH 15L with three applied pressures (50–110–170 MPa). The Quintus furnace can host two modules, which can provide different cooling rates, called Uniform Rapid Cooling (URC) and Uniform Rapid Quenching (URQ), respectively. Three of the samples were cooled with the URC module (HIP-Q-A). The achieved cooling rate, similar to that of the low-pressure furnace, was 162 °C/min. Two samples were treated with the URQ module (HIP-Q-B) achieving a cooling rate of 2450 °C/min (only 110 and 170 MPa were applied). After HIP-Q-A and HIP-Q-B at 110 MPa, the two samples underwent first aging at 1080 °C for 4 h, according to the recipe previously developed by the authors [7]. The reason for applying the first aging only to samples processed at 110 MPa is based on satisfactory densification results obtained within this paper, as described in further detail below.
- Three samples were heat treated in an air furnace at 1260 °C for 3 h and then cooled with an extremely low cooling rate, promoting the precipitation of coarse  $\gamma'$  particles. This condition was investigated to assess the effect of the solution annealing on a microstructure containing  $\gamma'$  particles obtained in an equilibrium condition, similar to an as-cast material. In other words, this condition was mainly investigated to evidence any difference resulting from the application of the HIP quench to an equilibrium microstructure with respect to that of an as-built sample consisting of an out-of-equilibrium and over-saturated solid solution coming from the extreme cooling rates applied during PBF-LB processes. More specifically, among the slow-cooled samples, one was used for the microstructural characterization, while the others were subjected to HIP-Q-A at 50 and 170 MPa, respectively.

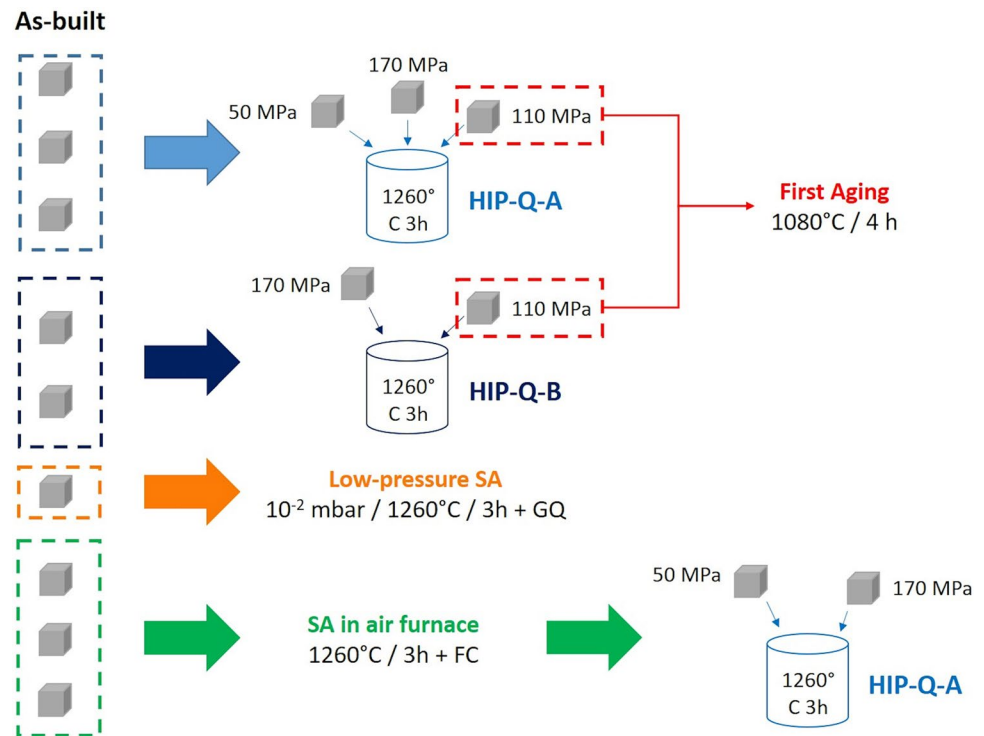
Figure 1 schematically represents the entire experimental test plane to assist the reader.

In other words, the main point of the green heat treatment (see Fig. 1) was to assess the solutioning capability

**Table 1** Nominal chemical composition of the commercial NI-1230 alloy used for this study

Element	Ni	Cr	Co	W	Ta	Mo	Al	Ti	Hf	Zr
Wt %	Bal	8.0	9.3	9.7	3.6	0.5	5.2	0.8	1.7	0.01

**Fig. 1** Descriptive scheme of all the performed heat treatments. GQ: gas quench, FC: furnace cooling



of the HIP quench, when a conventional microstructure with coarser  $\gamma'$  is considered (e.g., from investment casting). The samples with coarse  $\gamma'$  were hipped only at two pressure levels, i.e., the lower and the upper pressure limits (50 and 170 MPa, respectively), while the intermediate value was skipped to avoid material and energy wastage.

Figure 2 shows the obtained thermograms drawn during the cooling phase after HIP and traditional gas-quench. The cooling rate was recorded between the soaking temperature (1260 °C) and 400 °C, a temperature range where the cooling rate can be considered constant. Specifically, the temperatures were recorded with a type B thermocouple hosted in a hollow cylinder made of CM247 LC and used as a dummy. Hence, the plots refer to the tested material, not the surrounding gas. As can be seen, the orange curve shows a dramatic temperature drop achieved within the HIP equipped with the URQ module, while the blue one refers to the URC module. The grey curve shows the trend of the sample heat treated in the low-pressure furnace. The fact that the HIP and lower pressure furnace are intrinsically different pieces of equipment, and the difficulty in fine-tuning the cooling rate across the two, lead to the slight difference in cooling rates between HIP with URC module and the low-pressure gas quench. This condition is expected to slightly alter the particles' average size, as described in the following paragraphs of this work.

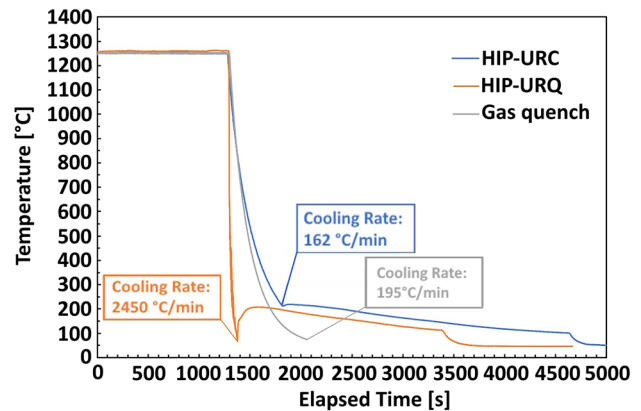


**Fig. 2** Cooling rates for different heat treatments: HIP with URQ module in orange, HIP with URC in blue, and traditional gas quench after low-pressure solution annealing in grey

### 2.3 Metallographic preparation

The microstructural characterization was performed along the XZ plane (parallel to the building direction). The samples were cut, ground, and polished up to 1  $\mu\text{m}$ : this procedure led to the “as-polished” surfaces being used for densification flaws assessment. A 0.04  $\mu\text{m}$  silica suspension was then used to improve the surface finishing of those samples intended for microstructural characterization. Chemical etching with Kalling #2 was applied to quantify  $\gamma'$  volume fraction, while electrolytic etching with a

30% vol. aqueous solution of  $\text{H}_3\text{PO}_4$  at 3.5 V was used to study the shape of the precipitates.

## 2.4 Densification flaws assessment

First, all the as-built samples were checked for process densification flaws. The procedure involved acquiring 15 images with a Leica DV500 light optical microscope (LOM) at 50 $\times$  on as-polished samples. Then a similar procedure was also applied to HIP-Q-A specimens. Since the only difference between HIP-Q-A and HIP-Q-B is the adopted cooling rate, only the first group of samples were analyzed. The assessment of HIPped density levels required a more refined observation technique: 30 images at 100 $\times$  per sample were taken to be sensitive to the extremely small size of flaws still visible. All the micrographs were processed using an algorithm developed in the ImageJ environment by the authors. Furthermore, the effectiveness of each HIP treatment in preventing the formation of any thermal induced porosity (TIPs) was assessed performing two heat treatments at 1260 °C for 2 and 4 h, indicated as HIP-Q + 2 h and HIP-Q + 4 h, respectively.

## 2.5 Grain size measurement

The grain size and structure of the samples after low-pressure solution annealing and HIP-Q-A were assessed with the LOM at 50 $\times$  after chemical etching with Kalling n<sup>o</sup>2. Each sample grain size was measured using the linear intercept method described in the ASTM E-112 standard. The direction parallel to the building direction is identified as “Z”, while the orthogonal one as “X”. The grain size was measured separately along Z and X directions, allowing for aspect ratio calculation.

## 2.6 $\gamma'$ assessment

The assessment of  $\gamma'$  precipitates' size in samples after HIP-Q-A was studied with a Zeiss EVO15 SEM. The  $\gamma'$  size was assessed averaging the results from five images taken at 10.000 $\times$  acquired with a backscattered electrons detector. The image analysis was performed running a dedicated script developed by the authors in the ImageJ environment. HIP-Q-B samples, due to finer  $\gamma'$  population, required, secondary electron images at 20.000 $\times$ , acquired with a Zeiss Merlin field-emission scanning electron microscope (FE-SEM). In this case, segmentation was obtained using a specific module contained in the ImageJ environment called “Trainable Weka Segmentation” (TWS) [32].

## 3 Results and discussion

### 3.1 The effect of the applied pressure on flaw volume fraction

Figure 3 shows the results obtained from the flaws assessment. The as-built sample defect level shows a large standard deviation. For this reason, the resulting data cloud is depicted as a grey area in the plot of Fig. 3. On the other hand, the green, red, and blue bars depict the densification flaws' fraction after HIP-Q, HIP-Q + 2 h, and HIP-Q + 4 h treatments, respectively.

All three applied pressures during HIP-Q treatment were effective in closing the defects population, which decreased from the average value of  $0.215 \pm 0.120\%$  in as-built condition to  $0.053 \pm 0.002\%$ ,  $0.057 \pm 0.001\%$ , and  $0.057 \pm 0.008\%$  after soaking at 1260 °C for 3 h applying 50, 110, and 170 MPa, respectively. This result highlights the possibility of effectively closing the densification flaws during the integrated treatment with 50 MPa of pressure, even if Lopez-Galilea et al. found a significant presence of retained cracks in PBF CMSX-4 alloy [25]. This result can be explained considering that the process parameters used during the manufacturing process limited the formation of cracks, and in general, the only defects present here were not connected to the surface and, thus, restorable during the HIP. As previously mentioned, applying a further solution annealing at 1260 °C did not cause severe thermal induced porosity (TIP) formation. Specifically, when 50 MPa are used, the defect level increases to  $0.073 \pm 0.016\%$  and  $0.056 \pm 0.025\%$  after being soaked for 2 and 4 h, respectively. Similar results were found in the other two conditions as depicted in the

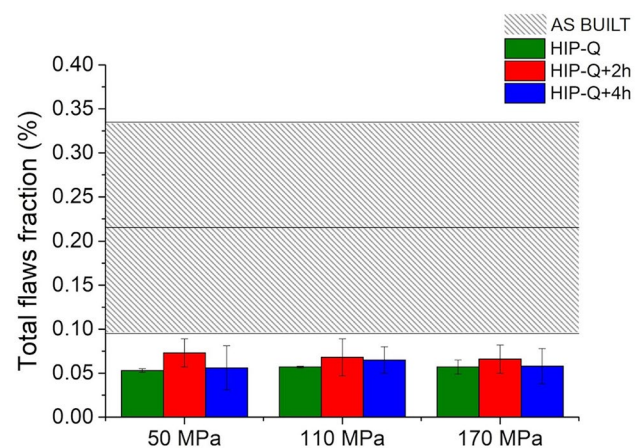


**Fig. 3** Flaws fraction measured for the samples after HIP-Q-A with different applied pressures (green bars). Red and blue bars represent the solution annealing samples after the additional HT at 1260 °C for 2 h and 4 h, respectively. These values are compared to the variability band measured on all the as-built samples (grey rectangle)

above bar chart. Considering the standard deviations, it can be concluded that all three pressures applied during HIP-Q effectively closed densification defects generating a stable structure against TIPs. The already good result observed in HIP-Q samples treated at 50 MPa can be explained considering two main points: first, the as-built samples already have a low fraction of defects, mainly located away from the surface. Second, applying a super-solvus HIP-Q treatment at 1260 °C guarantees optimal solid-state diffusion and a consistent plastic flow of the material, leading to an effective closure of the internal flaws [10]. Ultimately, the results demonstrate that no significant TIP formation could be observed even after 4 h of exposure, which is a consistent time to observe TIPs formation in Nickel superalloys [22]. However, the sample after HIP-Q at 50 MPa showed a slightly higher variation between the HIP-Q and the HIP-Q + 2 h conditions with respect to other studied cases. For this reason, a conservative approach was kept, and 110 MPa was chosen as the optimal pressure for the investigation of the first aging.

### 3.2 $\gamma'$ assessment after low-pressure solution annealing and HIP-Q-A (URC module)

First, electrolytic etching was used to reveal  $\gamma'$  morphology after its precipitation. To complete this task, the HIP-Q-A microstructure was compared with that of a sample solution annealing at the same temperature but in a low-pressure furnace (Fig. 4), this was considered helpful to evaluate if the pressure could have any influence during particles dissolution and precipitation.

Figure 4 shows the obtained microstructure after soaking and quenching the material without any further heat treatment. The left and right side of Fig. 4 shows  $\gamma'$  particles at low and higher magnification, respectively. More specifically, the right column of the picture focuses on the grain boundary morphology. Noteworthy, after low-pressure solution annealing and HIP-Q-A,  $\gamma'$  precipitates with a fan-like shape during the cooling process. Namely, at this stage, the typical regular and ordered cuboidal  $\gamma'$  structure of Nickel-based superalloys was not achieved. The qualitative general overview shows no significant morphological differences using different pressures during HIP-Q-A (Fig. 4c, e, g) and  $\gamma'$  is always irregular. Besides,  $\gamma'$  particles after low-pressure solution annealing (Fig. 4a, b) are slightly finer but still irregular. This size reduction shall be attributed to the faster cooling in the low-pressure furnace and not to the absence of applied pressure. This result proves that CM247 LC behaves differently with respect to other Ni-based systems, such as Astroloy, where previous studies demonstrated that cubic  $\gamma'$  particles could be obtained immediately after the solution annealing [33]. At the same time, this result is consistent with those obtained by Safari et al., who obtained slightly

irregular particles after solution annealing in a René 80 alloy obtained via traditional casting [13].

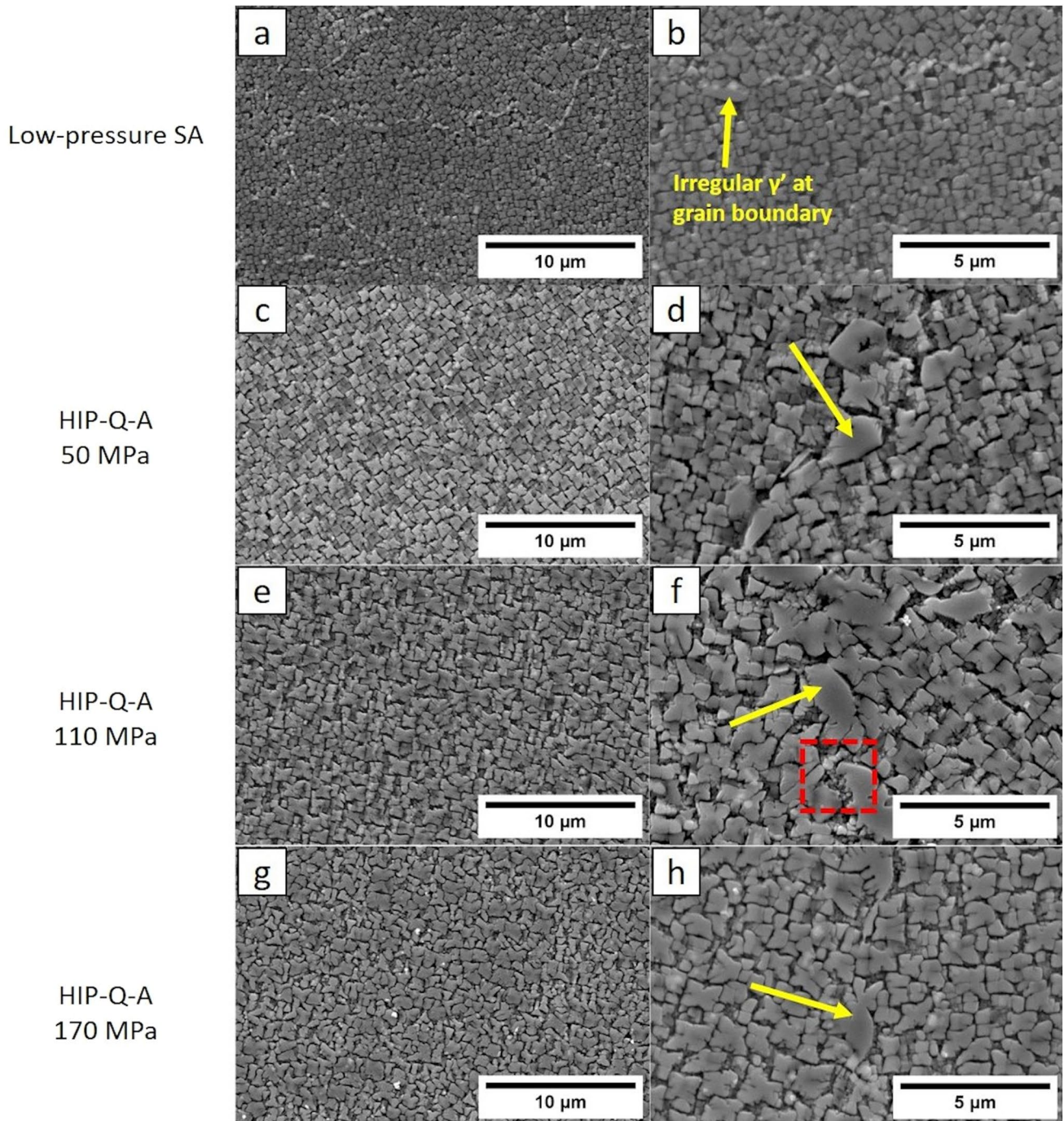
The alloys described in this paragraph (Astroloy and René 80) have slightly lower  $\gamma'$  fraction and different chemistry; despite this, they share with CM247 a cubic  $\gamma'$  pattern, indicating that all these alloys have a very similar lattice mismatch between the reinforcing particles and the matrix.

Figure 4b, d, f, h focuses on the material grain boundaries. Coarse and highly irregular  $\gamma'$  can be observed at the grain boundaries after low-pressure solution annealing and HIP-Q-A for all the applied pressures (yellow arrows in Fig. 4). The formation of highly irregular  $\gamma'$  at grain boundaries occurs during the cooling due to a process of growth and coarsening, which has been observed and described in a previous study on the continuous cooling of a Nickel superalloy by Qiu et al. [34]. Also in this case, the applied pressure does not significantly affect the morphology of these particles. Mainly secondary  $\gamma'$  particles can be observed within the grains. At the same time, a small amount of ternary  $\gamma'$  was found in the matrix channels, and its small volume fraction can be addressed considering that low-temperature aging treatments were not performed yet. The bimodal precipitation behavior in Nickel superalloy is linked to the occurrence of multiple nucleation bursts. Namely, first nucleation occurs at the beginning of the cooling, leading to coarser particles. In contrast, a second one occurs at lower temperatures to form the abovementioned small rounded nuclei [35, 36]. The first particles nucleate earlier, having a longer time to coarsen, while the latter ones have a much shorter time to grow, thus limiting their average size. At the same time, the competitive growth of  $\gamma'$  eases the coarsening of secondary particles rather than the nucleation of fresh nuclei. As a result, the smallest particles appear surrounded by larger ones as shown in the red dashed box of Fig. 4f.

Figure 5 shows the results obtained after image analysis with ImageJ. Considering the error bars, the precipitates' size is not significantly affected by the applied pressure, and the mean Feret diameter is  $471 \pm 205$ ,  $567 \pm 238$ , and  $527 \pm 231$  nm after HIP-Q-A applying 50, 110, and 170 MPa, respectively. Besides, a trend in the mean values could not be observed.

According to this analysis, the applied pressure during HIP-Q-A has limited or no influence on the final shape and size of  $\gamma'$ , which precipitates and grows with a fan-like shape.

Next, the HIP-Q-A was applied to the samples previously air-treated at 1260 °C for 2 h (green heat treatment in Fig. 1) and furnace-cooled (FC) to obtain coarse-equilibrium  $\gamma-\gamma'$  structure similar to that of a cast alloy. This test aims to verify if similar microstructures can be achieved by performing the HIP-Q-A on a material with an extremely coarse  $\gamma'$  obtained after the slow air cooling. This test was implemented to observe any difference with respect to the



**Fig. 4** Synoptic of  $\gamma'$  morphology for different solution annealing conditions. On the left, lower magnification images taken at 10,000 $\times$  after **a** low-pressure solution annealing and HIP-Q-A with applied pressure of **b** 50 MPa, **c** 110 MPa, and **d** 170 MPa. On the right,

higher magnification images with focus on the grain boundaries taken at 20,000 $\times$  after **b** low-pressure solution annealing and HIP-Q-A with applied pressure of **d** 50 MPa, **f** 110 MPa, and **h** 170 MPa

application of HIP-Q-A over an out-of-equilibrium microstructure as the one obtained through PBF-LB manufacturing. Considering the previous results and the almost negligible effect of the pressure on  $\gamma'$  formation, only two levels of pressure (50 and 170 MPa) were considered for this test.

The starting microstructure of the samples obtained after the (FC) was characterized by a very irregular and coarse  $\gamma'$  population with a Feret diameter above 1  $\mu\text{m}$  as shown in Fig. 6a. Besides, Fig. 6b, c show the microstructure after HIP-Q-A applying 50 and 170 MPa, respectively. The

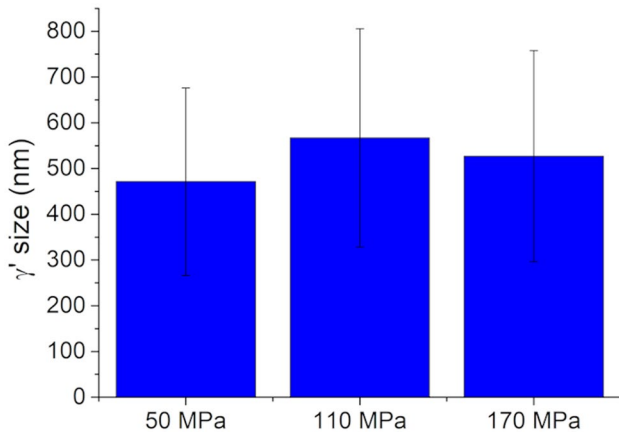


**Fig. 5** Effect of the different applied pressures on the  $\gamma'$  size after HIP-Q-A

HIP-Q-A successfully solubilized all the previous coarsened  $\gamma'$  particles and promoted further precipitation of new smaller particles. This effect could be seen indistinctly at both pressure levels, underlining that the applied pressure

does not significantly affect the solution process. Noteworthy,  $\gamma'$  particles were not cuboidal nor regular meaning that  $\gamma'$  shape after solutioning is also independent of the starting metallurgical condition, i.e., an over-saturated solid solution or a matrix with already formed precipitates.

### 3.3 $\gamma'$ assessment after HIP-Q-B (URQ module)

From a thermal perspective, HIP-Q-B is identical to HIP-Q-A, but an order of magnitude faster cooling rate was achieved at the end of this HIP cycle. This feature was considered a key factor for better understanding the precipitation process within CM247 LC. The fast-cooling rate achieved ( $\approx 2450$  °C/min) could freeze the nuclei of  $\gamma'$  immediately after their formation during the cooling, reducing their growth. Since cooling rate within URQ module is sensitive to the applied pressure, and a drastically slower rate was evidenced at 50 MPa, only 110 and 170 MPa were adopted during this stage of the study. The samples after HIP-Q-B were observed using the FE-SEM to resolve the extremely small  $\gamma'$  particles. Noteworthy, the applied cooling rate, even if extremely fast, could not suppress the precipitation of the

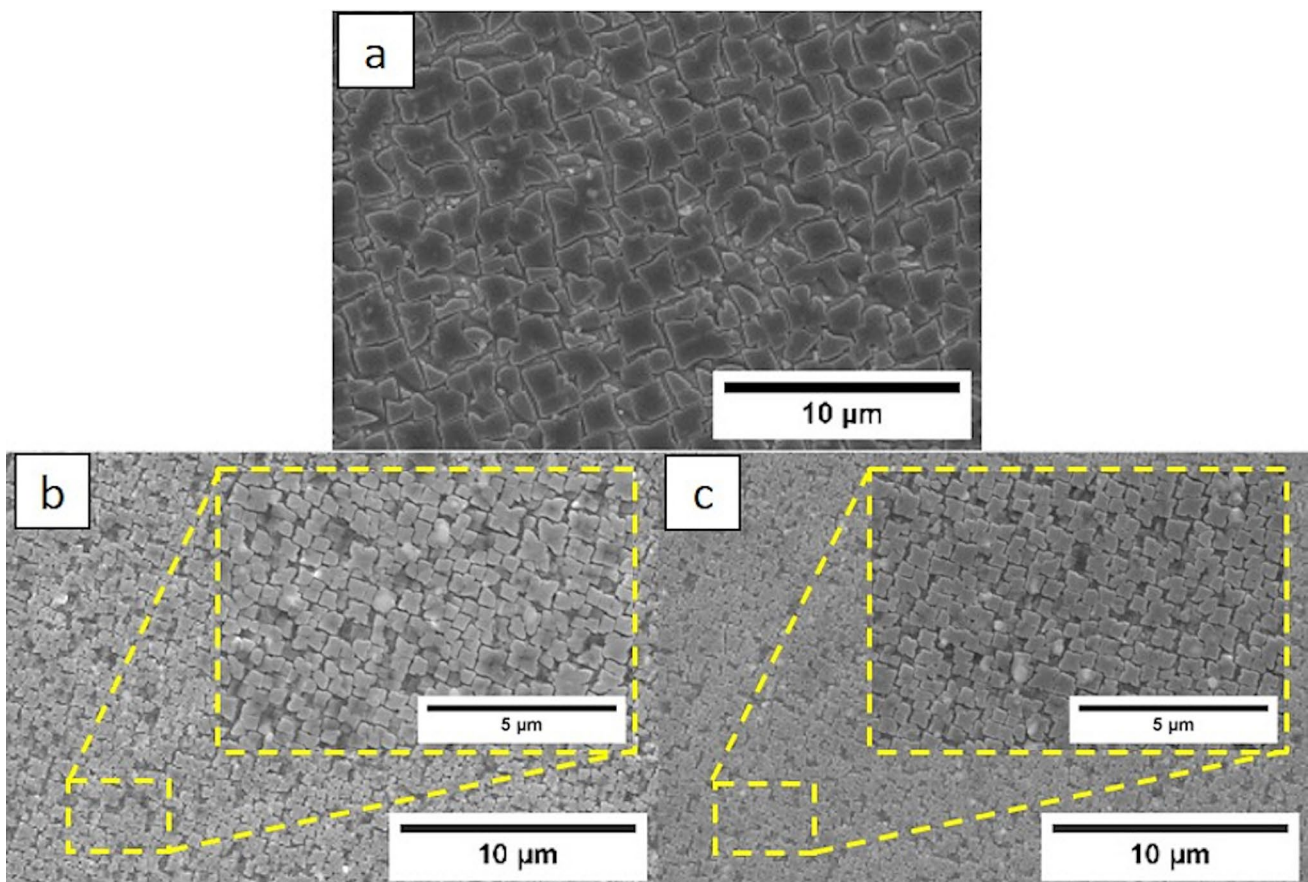


**Fig. 6**  $\gamma'$  morphological observation for as-built samples subjected to **a** heat treatment at 1260 °C for 3 h in air and further HIP-Q-A with applied pressures of **b** 50 MPa and **c** 170 MPa. Magnification: 10.000 $\times$  for lower magnification images and 25.000 $\times$  for inserts



reinforcing particles, a condition which is only achievable during BPF-LB solidification. A synoptic table is reported in Fig. 7. The  $\gamma'$  is more regular within the grains compared to the samples after HIP-Q-A (Fig. 7). Indeed, the URQ module used for the HIP-Q-B does not allow the particles to grow excessively and coarsen due to the diffusion time reduction [35]. However, their shape is still not regular and coarse particles (up to 1  $\mu\text{m}$ ) formed at the grain boundaries, as depicted by the yellow arrows in Fig. 7.

The results of the segmentation obtained using TWS tool in ImageJ are reported in Fig. 8. Considering the error bars, the results are almost identical, independently from the applied pressure during HIP-Q-B. The  $\gamma'$  size was  $160 \pm 72$  and  $147 \pm 67$  nm applying 110 and 170 MPa, respectively. Similarly to HIP-Q-A case, it is possible to conclude that dissolution and precipitation of  $\gamma'$  are little or no altered by the external pressure of the HIP.

The particles depicted in Fig. 7 demanded resolution through field-emission scanning electron microscopy (FESEM), using almost twice the magnification required for previous micrographs. As can be observed, while  $\gamma'$  precipitation was successfully achieved, the particle size was considerably reduced. The coarse particles found at

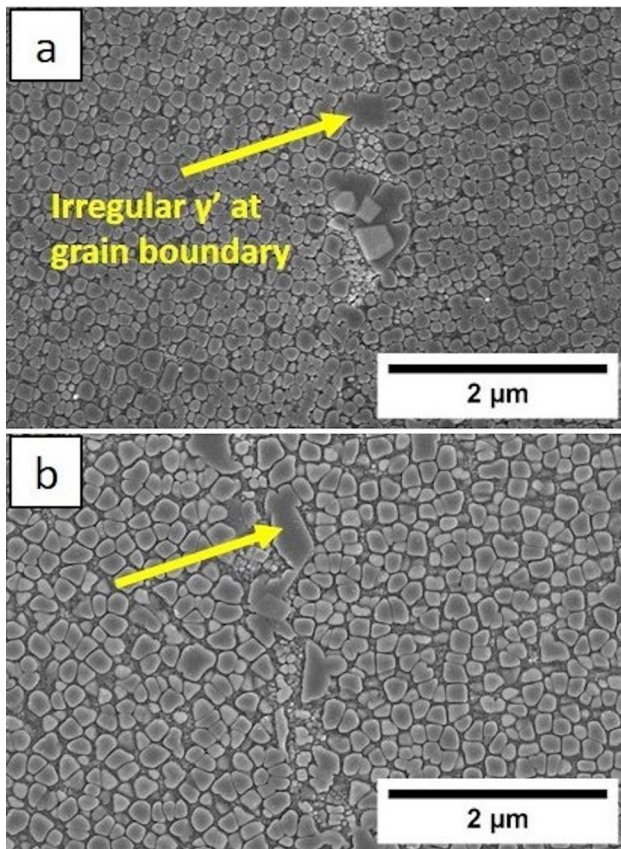


**Fig. 7** General overview of the  $\gamma'$  after HIP-Q-B with applied pressure of **a** 110 Mpa and **b** 170 MPa

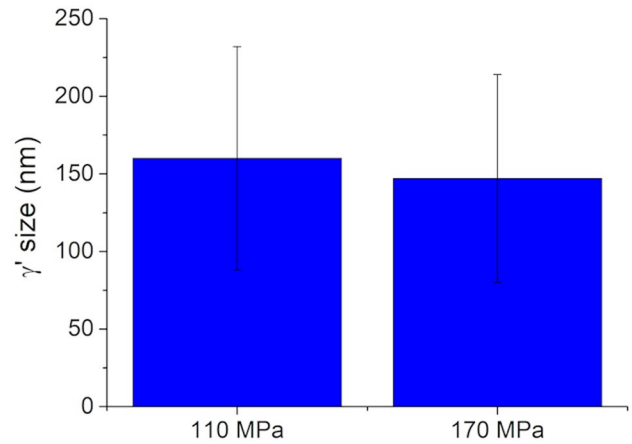


**Fig. 8** Effect of the different applied pressures on the  $\gamma'$  size after HIP-Q-B at 110 and 170 MPa

grain boundaries are presumed to be undissolved  $\gamma'$ , due to incomplete dissolution during the solution annealing stage. It is noteworthy to reiterate that, although the cooling rate in this process is rapid ca.  $2450^\circ\text{C}/\text{min}$ , it does not reach the levels attained during the solidification phase of a Laser Powder Bed Fusion (LPBF) process. Nevertheless, this cooling rate allows for the formation of  $\gamma'$  particles, resulting in a very fine and homogeneous particle distribution.

When cooling with the URQ module, the nucleation of  $\gamma'$  is favored compared to its growth. More specifically, less time is given to the diffusion processes, and the coarsening of the particles is limited [35]. Indeed, a higher fraction of very fine particles (a few tens of nm) could be observed in all the samples after HIP-Q-B (green arrows in Fig. 9) with respect to the HIP-Q-A case where the secondary  $\gamma'$  population was mostly mono-modal.

HIP-Q-B allowed to stop the growth of  $\gamma'$  immediately after its formation during cooling from the solution annealing temperature. As a result, after this test, it can be affirmed that applied pressure does not also affect the nucleation step of  $\gamma'$ . If the application of pressure had perturbed the precipitation of  $\gamma'$ , shifting its onset to longer times, the size or volume fraction of the particles would be different from case to case. The fact that the particles' size and fraction are similar in all the cases indicates that nucleation occurs at the same moment. In other words, a hypothetical  $\gamma'$  precipitation curve drawn on a continuous cooling transformation diagram would not be offset by the application of pressure during the HIP, thus giving rise to similar precipitation conditions during the cooling step. Finally, even freezing the microstructure at the end of HIP-Q-B did not lead to regular cubic precipitates, as observed in other systems [33].

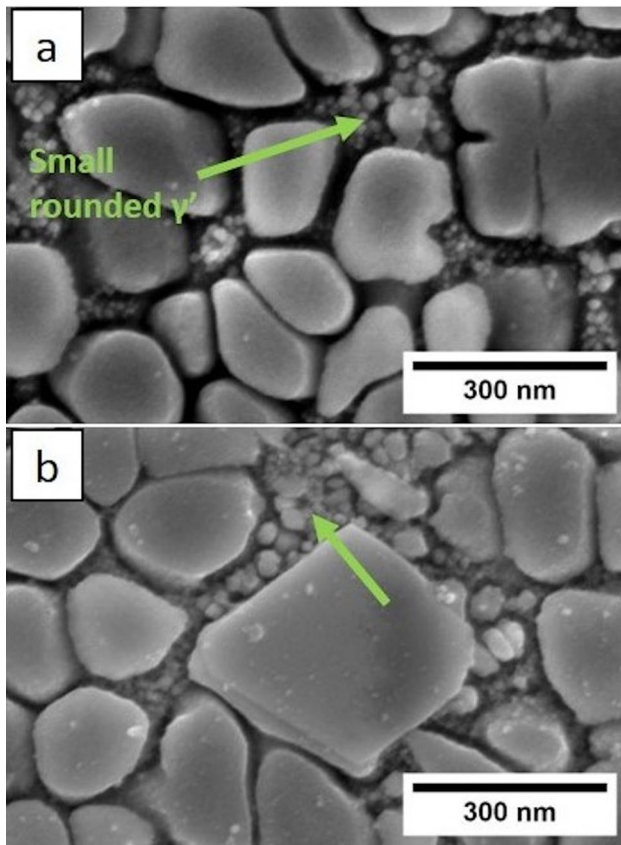


**Fig. 9** Presence of very fine  $\gamma'$  (tens of nm) precipitated in the channels between the larger precipitates observed after HIP-Q-B with applied pressure of **a** 110 MPa and **b** 170 MPa. Magnification: 300.000 $\times$

### 3.4 Grain size assessment

The samples after low-pressure solution annealing and HIP-Q-A were used to assess the grain size. Also in this case, the grain growth process is independent of the cooling rate, so HIP-Q-B samples were not considered. Figure 10a–d shows a synoptic table reporting the grain structure after solution annealing in the low-pressure furnace compared with HIP-Q samples at different pressures.

The grains are similar among the different treatment conditions. Some defects can be detected in the sample after low-pressure solution annealing (Fig. 10a) since no external pressure was applied during the solution annealing. Figure 10 shows that grains still have a certain degree of anisotropy along the building direction. On the other hand, Fig. 10e, f) depicts the effect of the applied pressure during solution annealing at 1260 °C on the grain size and aspect ratio of the alloy, respectively. The building direction is identified with the “Z”, while “X” represents a generic direction parallel to the deposited layer plane. The applied pressures during HIP-Q-A did not alter the grain size with

respect to the low-pressure solution annealing, considering the standard deviations. The grain size measured in Z direction is  $114 \pm 25 \mu\text{m}$  after low-pressure solution annealing, and it is  $116 \pm 14$ ,  $124 \pm 17$ , and  $128 \pm 21 \mu\text{m}$  after HIP-Q at 50, 110, and 170 MPa, respectively. Similarly, the X direction shows a grain size of  $69 \pm 9 \mu\text{m}$  for the low-pressure solution annealing sample and  $73 \pm 17$ ,  $73 \pm 11$ , and  $76 \pm 11 \mu\text{m}$  after solution annealing performed with an applied pressure of 50, 110, and 170 MPa, respectively. As a consequence, the aspect ratio of the grains calculated as Z-dir/X-dir is constant among the different conditions, and it results in  $1.7 \pm 0.2$  for the low-pressure solution annealing sample and  $1.6 \pm 0.3$ ,  $1.7 \pm 0.3$ , and  $1.7 \pm 0.2$  after HIP-Q at 50, 110, and 170 MPa, respectively. This result confirms that grain growth is a thermally activated process independent of external pressure [37]. These results comply with those presented above, where the dissolution of  $\gamma'$  was assessed after solution annealing at 1260 °C. At this temperature,  $\gamma'$  is completely dissolved, independently of the applied pressure during HIP-Q. For this reason, the pinning effect of  $\gamma'$  particles is removed, and  $\gamma$  grains are free to coarsen according to solid-state diffusion rules.

### 3.5 The effect of the first aging on the $\gamma'$ shape

The previous sections dealt with solution annealed samples and, more precisely, the results presented in Figs. 4 and 7 confirm that the  $\gamma'$  precipitates with irregular shape after solution annealing, independently from the applied pressure during the heat treatment or the cooling rate. For this reason, the two samples after HIP-Q-A and HIP-Q-B at 110 MPa underwent a first aging step at 1080 °C for 4 h, according to the recipe previously developed by the authors [7]. The first aging was performed to assess its role in the morphology of the  $\gamma'$  particles. The results are summarized in Fig. 11a, b, which show the microstructural evolution of samples HIP-Q-A and HIP-Q-B, respectively. The images clearly show  $\gamma'$  with a cubic shape, which is eventually achieved after this stage. The solid-state diffusion activated during the first aging step profoundly transformed the particles from irregular to cuboidal. The only noticeable difference is the final size of the particles, which are smaller in Fig. 11b, as a direct consequence of the finer microstructure, obtained after HIP-Q-B, as shown in Fig. 7b.

Based on the results of the present work, the evolution of the  $\gamma'$  after HIP-Q can be summarized in Fig. 12.

When cooling from the solution annealing temperature, a first nucleation burst occurs at higher temperatures, and the precipitates keep growing during the continuous cooling with different shapes depending on their nucleation site. Independently of the cooling rate, the diffusion of elements forming  $\gamma'$  appears particularly chaotic at this stage. The particles are forced to grow under a not clearly determined

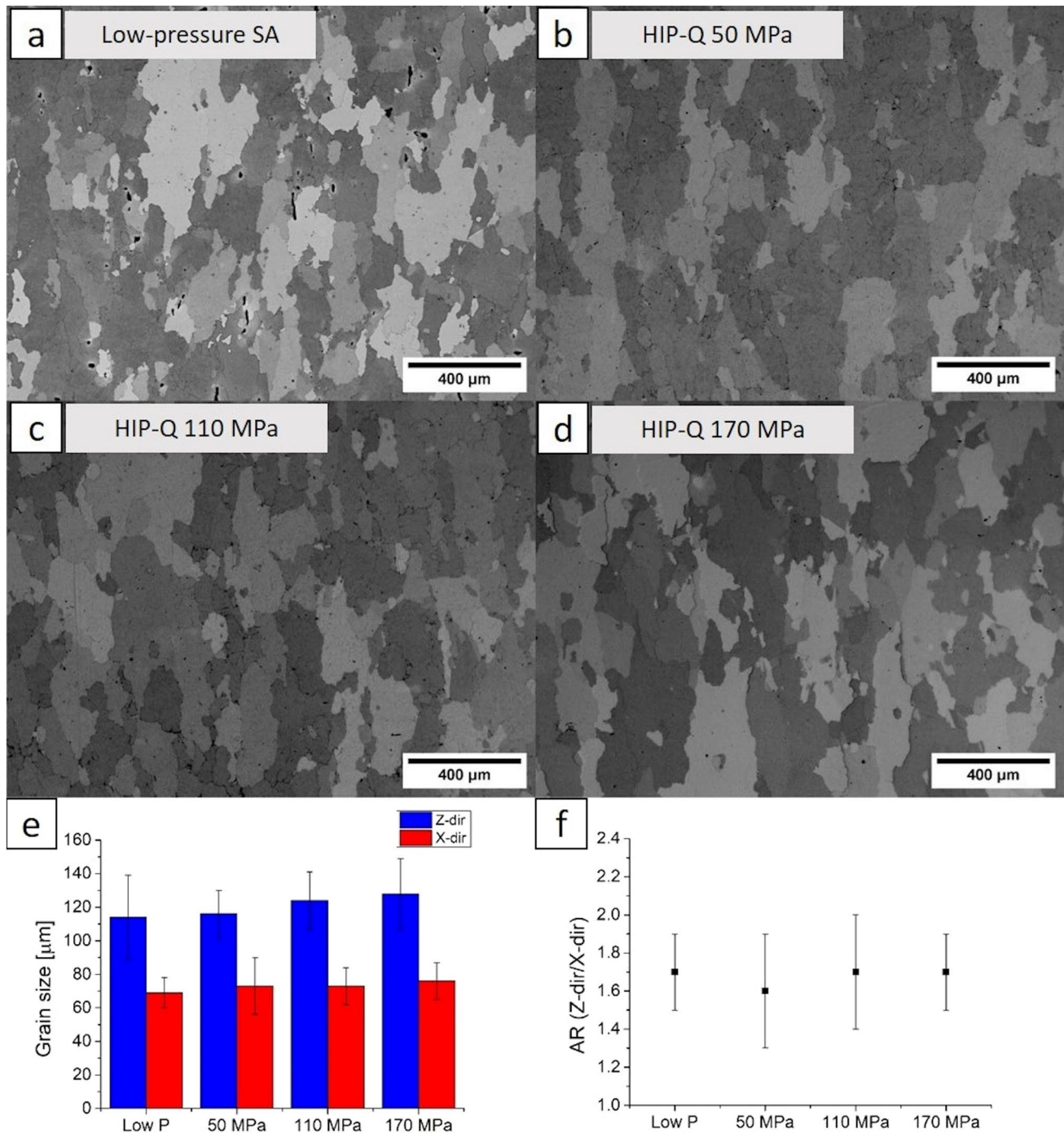


**Fig. 10** Grains morphology at 50 $\times$  after **a** low-pressure solution annealing and after HIP-Q-B with an applied pressure of **b** 50 MPa, **c** 110 MPa, and **d** 170 MPa. Below, the quantification results for **e** the grain size and **f** the aspect ratio are reported

compositional gradient which makes the interface between the matrix and the particles rounded. The diffusion rate is a function of the radius of the interface between  $\gamma$  and  $\gamma'$ . For this reason, some areas of  $\gamma'$  can grow faster than others depending on the local radius of the particle–matrix interface. This caused the formation of particles with an irregularly shaped profile and is schematized in the left panel of

Fig. 12a for grey and orange particles. This phenomenon is not happening at the grain boundary where diffusion is always faster, and particles (the light blue in the schematic) generally become coarser and irregular in Nickel-based superalloys. The precipitation behavior is similar from a pure morphological perspective during all the heat treatments. The only factor which can be altered with the heat

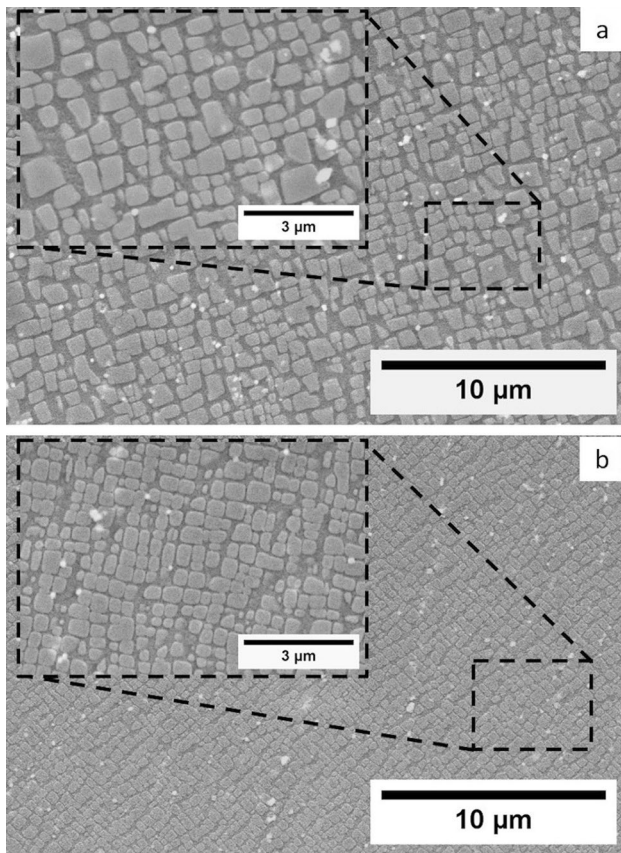


**Fig. 11** Morphological assessment of the  $\gamma'$  particles after first aging at 110 MPa after **a** HIP-Q-A and **b** HIP-Q-B. Magnification: 10.000 $\times$  for the main image and 30.000 $\times$  for the inserts

treatments is the size of the particles which is strictly a function of the adopted cooling rate. Finally, when the material undergoes the first aging step, the particles grow in a more controlled manner (Fig. 12b). The diffusion of  $\gamma'$  at 1080 °C is different. In this case, the diffusion of elements changes and allows the formation of an almost flat  $\gamma$ - $\gamma'$  interface, which is stably maintained during the first aging process, transforming irregular  $\gamma'$  particles into cuboidal ones. This main achievement demonstrates that first aging is crucial to reaching the optimal  $\gamma'$  shape in Nickel-based superalloys.

## 4 Conclusion

The effect of the applied pressure on the microstructure after super-solvus HIP quench at 1260 °C for 3 h was investigated in this study on a PBF-LB CM247 LC superalloy. More specifically, three pressures were studied: 50–110–170 MPa. A low-pressure solution annealing was also added as reference. The main outcomes are as follows:

- The tested pressures were effective in healing the PBF-LB densification flaw during HIP-Q and no significant thermal induced porosity (TIP) formation was measured after a following heat treatment at 1260 °C for 2 and 4 h.
- Irregular and mostly fan-like  $\gamma'$  was obtained after both low-pressure solution annealing and HIP-Q. In the latter case, neither the applied pressure nor the cooling rate (URC vs URQ) had significant effect on the  $\gamma'$  morphology. The applied pressure also had no effect on the  $\gamma'$  size. Indeed, it resulted in  $471 \pm 205$ ,  $567 \pm 238$ , and  $527 \pm 231$  nm applying 50, 110, and 170 MPa,

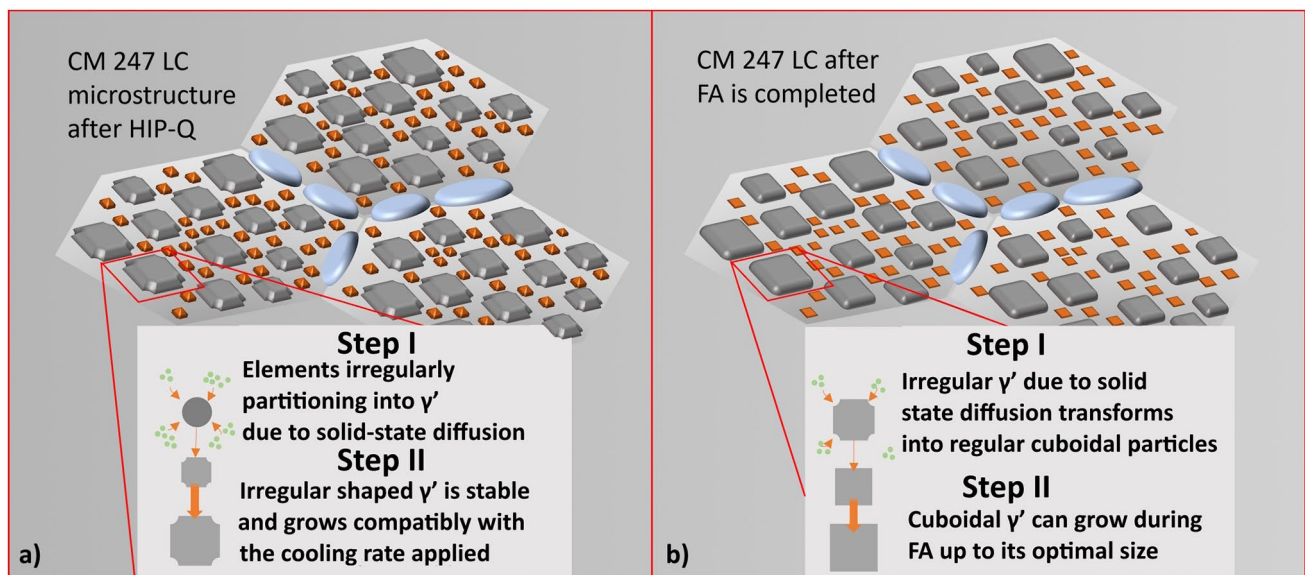


**Fig. 12** **a** Precipitation of  $\gamma'$  from the solution annealing temperature and **b** its evolution through following first aging

respectively, after HIP-Q-A. Similarly, for HIP-Q-B, it resulted in  $160 \pm 72$  and  $147 \pm 67$  nm applying 110 and 170 MPa, respectively.

- The HIP-Q-B led to a high fraction of very fine  $\gamma'$  in the inter-particles channels due to the extremely short time at disposal for their growth.
- As expected, the applied pressure had no visible effect on the grain coarsening because the applied temperature is effective in solutioning the  $\gamma'$  and  $\gamma$  grains are free to grow according to solid-state diffusion laws. Indeed, the grain size along the building direction was found between  $114 \pm 25$  and  $128 \pm 21$   $\mu\text{m}$  and between  $69 \pm 9$  and  $76 \pm 11$   $\mu\text{m}$  across the building direction. The aspect ratio of the grains was constant between  $1.6 \pm 0.3$  and  $1.7 \pm 0.3$ .
- After applying first aging at 1080 °C for 4 h, the optimal cubic-shaped  $\gamma'$  particles can be obtained. The size of the cubes is affected by the size of the original  $\gamma'$  particles precipitated during the cooling after solution annealing. The diffusion processes taking place in the sub-solvus regime of the first aging allows to reach flat  $\gamma$ – $\gamma'$  interface.

The current work proved that super-solvus HIP quench can be effectively applied to difficult-to-process PBF-LB Nickel-based superalloys like CM247 LC to heal the densification flaws and obtain a microstructure comparable to the traditional low-pressure solution annealing treatments. The consolidation and solution annealing steps can be integrated and this result can have a significant industrial importance to contain the gas and electric energy consumptions during HIP, reducing the total cycle time with significant and positive environmental effects, besides the productivity benefit.

**Acknowledgement** The authors wish to thank Dr. Flaviana Calignano, Associate Professor at Politecnico di Torino, IAM@Polito Interdepartmental Center, for her precious support given during the preparation and development of the manufacturing process.

**Author contributions** Data curation: Pietro Antonio Martelli, Pietro Antonio Martelli; investigation: Pietro Antonio Martelli; software: Pietro Antonio Martelli; writing—original draft: Pietro Antonio Martelli; writing—review: Emilio Bassini; conceptualization: Emilio Bassini; formal analysis: Emilio Bassini; methodology: Emilio Bassini; supervision: Emilio Bassini, Daniele Ugues; validation: Emilio Bassini, Daniele Ugues.

**Funding** Open access funding provided by Politecnico di Torino within the CRUI-CARE Agreement. This research did not receive any specific grant from funding agencies in the public, commercial, or not-for-profit sectors.

**Data availability** All the experimental data to reproduce these findings are already contained in the paper and further material can be disclosed contacting the corresponding author.

## Declarations

**Conflict of interest** The authors declare that they have no known competing financial interests or personal relationships that could have appeared to influence the work reported in this paper.

**Open Access** This article is licensed under a Creative Commons Attribution 4.0 International License, which permits use, sharing, adaptation, distribution and reproduction in any medium or format, as long as you give appropriate credit to the original author(s) and the source, provide a link to the Creative Commons licence, and indicate if changes were made. The images or other third party material in this article are included in the article's Creative Commons licence, unless indicated otherwise in a credit line to the material. If material is not included in the article's Creative Commons licence and your intended use is not permitted by statutory regulation or exceeds the permitted use, you will need to obtain permission directly from the copyright holder. To view a copy of this licence, visit <http://creativecommons.org/licenses/by/4.0/>.

## References

1. Donachie MJ, Donachie SJ (2002) Superalloys: a technical guide. <https://doi.org/10.1016/B978-0-444-43022-9.50017-1>
2. Tan C, Weng F, Sui S, Chew Y, Bi G (2021) Progress and perspectives in laser additive manufacturing of key aeroengine materials. *Int J Mach Tools Manuf* 170:103804. <https://doi.org/10.1016/j.ijmactools.2021.103804>
3. Martelli PA, Sivo A, Calignano F, Bassini E, Biamino S, Ugues D (2023) Parameters optimization and repeatability study on low-weldable nickel-based superalloy René 80 processed via laser powder-bed fusion (L-PBF). *Metals* 13:210. <https://doi.org/10.3390/met13020210>
4. Marchese G, Bassini E, Calandri M, Ambrosio EP, Calignano F, Lorusso M, Manfredi D, Pavese M, Biamino S, Fino P (2016) Microstructural investigation of as-fabricated and heat-treated Inconel 625 and Inconel 718 fabricated by direct metal laser sintering: contribution of Politecnico di Torino and Istituto Italiano di Tecnologia (IIT) di Torino. *Met Powder Rep* 71:273–278. <https://doi.org/10.1016/j.mprp.2016.06.002>
5. Markanday JFS, Christofidou KA, Miller JR, Livera ER, Jones NG, Pickering EJ, Li W, Pardi Y, Jones CN, Stone HJ (2023) The microstructural evolution of CM247LC manufactured through laser powder bed fusion. *Metall Mater Trans A Phys Metall Mater Sci* 54:1758–1775. <https://doi.org/10.1007/s11661-022-06939-0>
6. Carter LN, Essa K, Attallah MM (2015) Optimisation of selective laser melting for a high temperature Ni-superalloy. *Rapid Prototyp J* 21:423–432. <https://doi.org/10.1108/RPJ-06-2013-0063>
7. Bassini E, Sivo A, Martelli PA, Rajczak E, Marchese G, Calignano F, Biamino S, Ugues D (2022) Effects of the solution and first aging treatment applied to as-built and post-HIP CM247 produced via laser powder bed fusion (LPBF). *J Alloys Compd* 905:164213. <https://doi.org/10.1016/j.jallcom.2022.164213>
8. Wei Q, Xie Y, Teng Q, Shen M, Sun S, Cai C (2022) Crack types, mechanisms, and suppression methods during high-energy beam additive manufacturing of nickel-based superalloys: a review. *Chin J Mech Eng Addit Manuf Front* 1:100055. <https://doi.org/10.1016/j.cjmeam.2022.100055>
9. Miller JR, Markanday JFS, Fairclough SM, Wise GJ, Rae CMF, Owen LR, Stapleton D, D'Souza N, Bagot PAJ, Stone HJ (2024) Gamma prime precipitation in as-deposited Ni-based superalloy IN713LC. *Scr Mater* 239:115775. <https://doi.org/10.1016/j.scripamat.2023.115775>

10. Atkinson HV, Davies S (2000) Fundamental aspects of hot isostatic pressing: an overview. *Metall Mater Trans A Phys Metall Mater Sci* 31:2981–3000. <https://doi.org/10.1007/s11661-000-0078-2>
11. Nguyen L, Shi R, Wang Y, De Graef M (2016) Acta materialia quantification of rafting of  $\gamma'$  precipitates in Ni-based superalloys. *Acta Mater* 103:322–333. <https://doi.org/10.1016/j.actamat.2015.09.060>
12. Van Sluytman JS, Pollock TM (2012) Optimal precipitate shapes in nickel-base  $\gamma$ - $\gamma'$  alloys. *Acta Mater* 60:1771–1783. <https://doi.org/10.1016/j.actamat.2011.12.008>
13. Safari J, Nategh S (2006) On the heat treatment of Rene-80 nickel-base superalloy. *J Mater Process Technol* 176:240–250. <https://doi.org/10.1016/j.jmatprotec.2006.03.165>
14. Qin XZ, Guo JT, Yuan C, Hou JS, Zhou LZ, Ye HQ (2012) Long-term thermal exposure responses of the microstructure and properties of a cast Ni-base superalloy. *Mater Sci Eng A* 543:121–128. <https://doi.org/10.1016/j.msea.2012.02.059>
15. Xu J, Brodin H, Peng RL, Luzin V, Moverare J (2022) Effect of heat treatment temperature on the microstructural evolution of CM247LC superalloy by laser powder bed fusion. *Mater Charact* 185:111742. <https://doi.org/10.1016/j.matchar.2022.111742>
16. Newell DJ, O'Hara RP, Cobb GR, Palazotto AN, Kirka MM, Burggraf LW, Hess JA (2019) Mitigation of scan strategy effects and material anisotropy through supersolvus annealing in LPBF IN718. *Mater Sci Eng A* 764:138230. <https://doi.org/10.1016/j.msea.2019.138230>
17. Viswanathan GB, Banerjee R, Singh A, Nag S, Tiley J, Fraser HL (2011) Precipitation of ordered phases in metallic solid solutions: a synergistic clustering and ordering process. *Scr Mater* 65:485–488. <https://doi.org/10.1016/j.scriptamat.2011.06.002>
18. Weddeling A, Theisen W (2017) Energy and time saving processing: a combination of hot isostatic pressing and heat treatment. *Met Powder Rep* 72:345–348. <https://doi.org/10.1016/j.mprp.2016.04.001>
19. Ahlfors M (2019) High pressure heat treatment of AM parts—combining HIP and heat treatment, 30th ASM heat treating society conference and exposition. *Heat Treat* 2019—Ext. Abstr. 2, pp 11–17. <https://doi.org/10.31399/asm.cp.ht2019p0011>
20. Rezaei A, Madaah Hosseini HR (2017) Evolution of microstructure and mechanical properties of Al-5 wt% Ti composite fabricated by P/M and hot extrusion: effect of heat treatment. *Mater Sci Eng A* 689:166–175. <https://doi.org/10.1016/j.msea.2017.02.049>
21. Niklas A, Orden S, Bakedano A, da Silva M, Nogués E, Fernández-Calvo AI (2016) Effect of solution heat treatment on gas porosity and mechanical properties in a die cast step test part manufactured with a new AlSi10MnMg(Fe) secondary alloy. *Mater Sci Eng A* 667:376–382. <https://doi.org/10.1016/j.msea.2016.05.024>
22. Bu H, Chen L, Duan Y (2022) Effect of solution heat treatment on the porosity growth of nickel-based P/M superalloys. *Metals* 12:1973. <https://doi.org/10.3390/met12111973>
23. Amirjan M, Sakiani H (2019) Effect of scanning strategy and speed on the microstructure and mechanical properties of selective laser melted IN718 nickel-based superalloy. *Int J Adv Manuf Technol* 103:1769–1780. <https://doi.org/10.1007/s00170-019-03545-0>
24. Mujica Roncery L, Lopez-Galilea I, Rutttert B, Bürger D, Wolgramm P, Eggeler G, Theisen W (2016) On the effect of hot isostatic pressing on the creep life of a single crystal superalloys. *Adv Eng Mater* 18:1381–1387. <https://doi.org/10.1002/adem.201600071>
25. Lopez-Galilea I, Rutttert B, He J, Hammerschmidt T, Drautz R, Gault B, Theisen W (2019) Additive manufacturing of CMSX-4 Ni-base superalloy by selective laser melting: influence of processing parameters and heat treatment. *Addit Manuf* 30:100874. <https://doi.org/10.1016/j.addma.2019.100874>
26. Meid C, Dennstedt A, Ramsperger M, Pistor J, Rutttert B, Lopez-Galilea I, Theisen W, Körner C, Bartsch M (2019) Effect of heat treatment on the high temperature fatigue life of single crystalline nickel base superalloy additively manufactured by means of selective electron beam melting. *Scr Mater* 168:124–128. <https://doi.org/10.1016/j.scriptamat.2019.05.002>
27. Goel S, Ahlfors M, Bahbou F, Joshi S (2019) Effect of different post-treatments on the microstructure of EBM-built alloy 718. *J Mater Eng Perform* 28:673–680. <https://doi.org/10.1007/s11665-018-3712-0>
28. Angré A, Ahlfors M, Chasoglou D, Larsson L, Claesson E, Karlsson O (2017) Phase transformation under isostatic pressure in HIP. *Powder Metall* 60:167–174. <https://doi.org/10.1080/00325899.2017.1318479>
29. Peters S, Perez M, Blackwell P (2023) Integrating HIP and homogenisation heat treatment and its effect on workability of a conventional peritectic TiAl alloy. *Intermetallics* 158:107884
30. Mujica Roncery L, Lopez-Galilea I, Rutttert B, Huth S, Theisen W (2016) Influence of temperature, pressure, and cooling rate during hot isostatic pressing on the microstructure of an SX Ni-base superalloy. *Mater Des* 97:544–552. <https://doi.org/10.1016/j.matdes.2016.02.051>
31. Lopez-Galilea I, Hecker L, Epishin A, Bürger D, Rutttert B, Thome P, Weber S, Theisen W (2023) Super-solidus hot isostatic pressing heat treatments for advanced single crystal Ni-base superalloys. *Metall Mater Trans A Phys Metall Mater Sci* 54:1509–1525. <https://doi.org/10.1007/s11661-022-06884-y>
32. Arganda-Carreras I, Kaynig V, Rueden C, Eliceiri KW, Schindelin J, Cardona A, Seung HS (2017) Trainable Weka segmentation: a machine learning tool for microscopy pixel classification. *Bioinformatics* 33:2424–2426. <https://doi.org/10.1093/bioinformatics/btx180>
33. Bassini E, Marchese G, Cattano G, Lombardi M, Biamino S, Ugues D, Vallillo G, Picqué B (2017) Influence of solutioning on microstructure and hardness of hot isostatically pressed astroloy. *J Alloys Compd* 723:1082–1090. <https://doi.org/10.1016/j.jallcom.2017.06.332>
34. Qiu CL, Andrews P (2013) On the formation of irregular-shaped gamma prime and serrated grain boundaries in a nickel-based superalloy during continuous cooling. *Mater Charact* 76:28–34. <https://doi.org/10.1016/j.matchar.2012.11.012>
35. Singh ARP, Nag S, Hwang JY, Viswanathan GB, Tiley J, Srinivasan R, Fraser HL, Banerjee R (2011) Influence of cooling rate on the development of multiple generations of  $\gamma'$  precipitates in a commercial nickel base superalloy. *Mater Charact* 62:878–886. <https://doi.org/10.1016/j.matchar.2011.06.002>
36. Singh ARP, Nag S, Chattopadhyay S, Ren Y, Tiley J, Viswanathan GB, Fraser HL, Banerjee R (2013) Mechanisms related to different generations of  $\gamma'$  precipitation during continuous cooling of a nickel base superalloy. *Acta Mater* 61:280–293. <https://doi.org/10.1016/j.actamat.2012.09.058>
37. Moore II, Taylor JI, Tracy MW, Burke MG, Palmiere EJ (2017) Grain coarsening behaviour of solution annealed alloy 625 between 600–800 °C. *Mater Sci Eng A* 682:402–409. <https://doi.org/10.1016/j.msea.2016.11.060>

**Publisher's Note** Springer Nature remains neutral with regard to jurisdictional claims in published maps and institutional affiliations.